Structural, mechanical, and magnetic properties of ferrite–austenite mixture in evaporated 304 stainless steel thin films

Noureddine Merakeb, Amel Messai, Abdelkader Djelloul & Ahmad I. Ayesh

Applied Physics A
Materials Science & Processing

ISSN 0947-8396

Appl. Phys. A
DOI 10.1007/s00339-015-9472-x

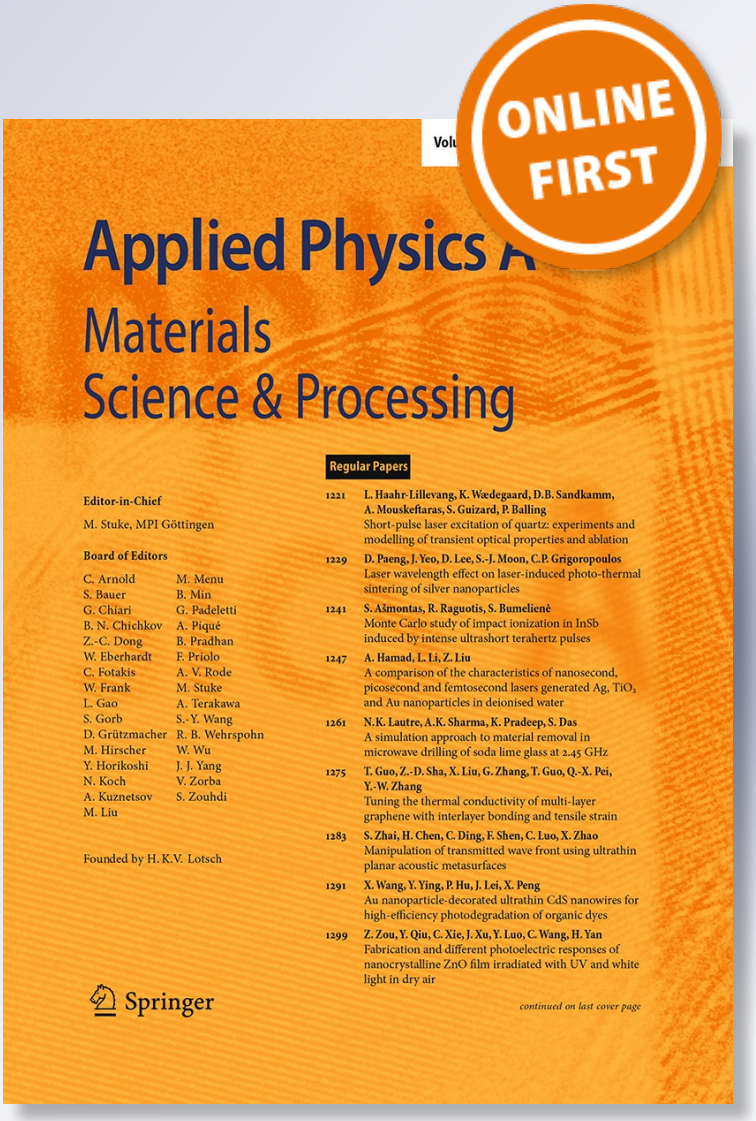

Springer

Appl. Phys. A
DOI 10.1007/s00339-015-9472-x

Applied Physics A
Materials Science & Processing

Structural, mechanical, and magnetic properties of ferrite–austenite mixture in evaporated 304 stainless steel thin films

Noureddine Merakeb[1] · Amel Messai[2] · Abdelkader Djelloul[2] · Ahmad I. Ayesh[3]

Received: 29 June 2015 / Accepted: 31 August 2015

Abstract In this paper, we investigate the structure, composition, magnetic, and mechanical properties of stainless steel thin films formed by thermal evaporation technique. These thin films reveal novel structural and physical properties where they were found to consist of nanocrystals that are ~90 % body-centred cubic crystal structure which holds ferromagnetic properties (α-phase), and ~10 % face-centred cubic crystal structure which is paramagnetic at room temperature (γ-phase). The presence of the above phases was quantified by X-ray diffraction, transmission electron microscopy, and conversion electron Mössbauer spectroscopy. The magnetic properties were evaluated by a superconducting quantum interference device magnetometer, and they confirmed the dual-phase crystal structure of the stainless thin films, where the presence of γ-phase reduced the magnetization of the produced thin films. In addition, the fabricated stainless steel thin films did not contain micro-cracks, and they exhibit a tensile stress of about 1.7 GPa, hardness of 7.5 GPa, and elastic modulus of 104 GPa.

✉ Ahmad I. Ayesh
ayesh@qu.edu.qa

[1] Metallurgy and Materials Engineering Laboratory, Sciences Engineer Faculty, Badji Mokhtar Annaba - University, P.O. Box 12, 23000 Annaba, Algeria

[2] Laboratoire des Structures, Propriétés et Interactions Inter Atomiques (LASPI2A), Institut des Sciences et Technologie Université Abbes Laghrour Khenchela, 40000 Khenchela, Algeria

[3] Department of Mathematics, Statistics and Physics, Qatar University, Doha, Qatar

1 Introduction

Bulk 304 stainless steel is a highly demanded material in industry due to its novel properties and wide range of applications [1–3]. The main advantages of stainless steel over other metals are: its resistance to corrosion in severe environments, it holds outstanding mechanical properties at widespread temperature range, and its low oxidation rate at high temperatures [4–6]. The superior properties of bulk 304 stainless steel are assigned to its microstructure that consists of a unique austenite phase [7, 8]. The austenite phase is paramagnetic [9], while the ferrite phase is ferromagnetic when measured at room temperature [10].

Thin films of stainless steel exhibit a main advantage over their bulk which is the formation of a protective passive film on the surface of the sample [11, 12]. Different morphology characterization techniques were used recently to characterize the crystal structure, composition, and grain size of stainless steel thin films [13, 14]. The combination of X-ray diffraction (XRD) and transmission electron microscopy (TEM) provides a powerful tool to quantify the crystal structure of granular systems.

Bulk 304 stainless steel (AISI 304 type) is normally non-ferromagnetic, and it exhibits FCC austenite structure (γ-phase) at ambient temperature [15]. On contrast, stainless steel thin films fabricated by the physical vapour deposition (PVD) method are strongly ferromagnetic and they exhibit BCC ferrite structure (α-phase) at ambient temperature [16–19]. However, this is an unstable polycrystalline structure for thin films formed by PVD method because of the ultra-quick cooling of the atomic vapour when deposited on a substrate [16].

Previously, we presented results of a comparative study of the microstructural stainless steel thin films fabricated by two PVD methods: ion beam sputtering and the thermal

Published online: 04 September 2015

evaporation [20]. The study demonstrated the existence of two ferromagnetic iron sites in the ferrite BCC (α-phase) of the stainless steel thin films fabricated by thermal evaporation only [21]. The effects of annealing and addition of titanium on the structural properties of these thin films were investigated. Further investigation is needed to address the crystal structure, structure size, composition, magnetization, and mechanical properties.

In this study, stainless steel thin films are fabricated by the thermal evaporation method which is, relatively, a simple PVD technique. The structure, composition, mechanical, and magnetic properties of the thin films are investigated in details using: conversion electron Mössbauer spectroscopy (CEMS), XRD, TEM, scanning electronic microscope (SEM), and energy-dispersive X-ray analysis (EDX). The magnetization is investigated using a superconducting quantum interference device (SQUID), while the mechanical properties are tested using a nanoindenter. In the following section, the experimental procedure used in this work is described. Next, the results are presented followed by a detailed discussion.

2 Experimental

2.1 Thin film fabrication

Stainless steel thin films were prepared by thermal evaporation on substrates that were placed vertically above the thermal evaporation source (vertical distance of $\sim$20 cm) in a residual pressure of approximately 4×10^{-6} mbar. The evaporation temperature of bulk stainless steel was $<$1400 °C, and deposition speed was $V_d = 103$ Å/s. The substrates were fixed on a non-rotating table that was kept at room temperature ($\sim$25 °C). The bulk source material was a commercial AISI 304 austenitic stainless steel. For evaporation, a stainless steel plate was cut mechanically into small chips ($3 \times 1.5 \times 0.5$ mm^3). The chips and the surface of the substrates were cleaned with alkaline detergent and alcohol by means of ultrasonic bath before deposition.

Thermal evaporation was used to produce stainless steel thin films with thicknesses of 100–200 nm onto the following substrates: glass, quartz, and Si wafers (crystal orientation [100]) with native oxide. A custom-designed deposition chamber was employed in this work which utilized a tungsten crucible, and a quartz crystal to monitor and control the film thickness. The thicknesses of the stainless steel thin films were confirmed by: (i) a Stylus RM 600 laser profilometer at a resolution of 5 nm (non-contact method) and (ii) mechanical Dektak IIA profilometer using the scanning mode (contact method). In this study, thin films of a thickness of 160 nm were used.

2.2 Characterization techniques

2.2.1 XRD

XRD analyses of the stainless steel thin films were performed using a SIEMENS D500/501 diffractometer (Cu-Kα radiation, $\lambda = 1.5406$ Å) with a step size of 0.05°/s. XRD data were collected over a 2θ range of 40–130°. The diffractometer was equipped with a graphite monochromator placed before the detector to eliminate Kβ radiation.

2.2.2 TEM

The structure of the prepared thin films was investigated using a JEOL 200-CX TEM. Herein, bulk austenitic stainless steel was evaporated on TEM grids with a thickness of about 100 nm. TEM was utilized in this work for electron diffraction (that determines crystal structure) and imaging, i.e. bright and dark field modes. The TEM was operated under a pressure of $\sim 10^{-6}$ mbar using an accelerating voltage of 200 kV with a resolution of 0.4 nm for imaging and 0.0251 Å of the wavelength for electron diffraction.

2.2.3 CEMS

Room-temperature CEMS spectra were recorded using a constant acceleration spectrometer, with a 57 Co/Rh source (50 mCi) and a continuous gas flow proportional counter (using He and 5 % CH_4 gases at 293 K) [22]. The Mössbauer technique enables examining atomic coordination in the neighbourhood of probe nuclei via hyperfine interaction parameters. The spectra were computer fitted which yielded the hyperfine magnetic field (HMF) distribution, where it was assumed that each spectrum is a superposition of a number of sub-spectra having different hyperfine interactions and relative contributions. In all cases, the isomer shift at the 57 Fe nucleus is given relative to a-Fe at room temperature.

2.2.4 SEM and EDX

A scanning electron microscope (JEOL 5600-2v) was utilized to investigate the morphology of the produced thin films using an accelerating voltage of 20 kV. The composition of the thin films was also determined by EDX analysis inside the SEM chamber. The chemical composition of the bulk stainless steel and thin films was measured and shown in Table 1.

2.2.5 SQUID

Magnetization measurements were performed with a magnetic field (H) in the plane of thin film surface, using a

Table 1 Chemical compositions of the stainless steel nanocrystalline thin film and the initial bulk material

Elements	Chemical composition (weight %)	
	Bulk (304) stainless steel	Nanocrystalline stainless steel thin films
Fe	70.95	71.75
Cr	18.98	17.06
Ni	7.96	7.60
Mn	1.70	3.48
Si	0.41	–
C	0.05	–

superconducting quantum interference device with an MPMS-XL7 magnetometer (Quantum Design). The surface area of each thin film specimen used for magnetization measurements was 4×5 mm^2.

2.2.6 *Residual stress*

Residual stress was determined for the thin films by the ($\sin^2 \psi$) method using the obtained XRD results, where ψ is the angle between the normal to sample surface and the normal to diffraction plan (hkl). The $\sin^2 \psi$ method is appropriate for constraints measurement of thin films because those thin films consist of homogenous fine crystals with random orientations. This method is based on the relation between the d_{hkl} reticular distance and the variation in ψ angle (i.e. d_{ψ}, $d_{\psi=0}$, and $d_{+\psi}$), where ψ changes between $-45°$ and $+45°$. The relation between (ln (1/sin θ)) and ($\sin^2 \psi$) provides a linear relationship, and the slope of the linear fit is $m = ½\ S_2\ \sigma\varphi$. Here, S_2 is an elastic constant, σ is the residual stress of the sample surface, and φ is an angle defining the direction of deformation and strain chosen between the x and y directions relative to the sample surface. The $\sin^2 \psi$ method was applied for the Bragg's peak of the (211) α-phase, where $\psi = 0$ corresponds to $2\theta = 82.696°$ with FWHM $= 0.846°$. For each ψ angle value, we measured the new position of 2θ angle for peak (211) α-phase. The values of ψ angle used in this study are shown in Table 2.

2.2.7 *Nanoindentation*

The experimental nanoindentation method allows studying the elasto-plastic properties of nanometric scale of thin films. A NHT100 (CSM Instruments of Suisse) nanoindenter with a displacement precision of 0.3 nm was used in this study. The nanoindenter used a Berkovitch's pyramidal diamond penetration tool with $\varepsilon = 0.75$ (geometrical constant of indenter). The maximum load was 0.5 mN, and it was applied on indenter which was sufficient to ensure a penetration depth of around 10 % of film thickness (in order to avoid substrate scratch/damage, or unrepresentative measurements that are influenced by the substrate). The hardness and elastic modulus values were determined using load and displacement results after treatment of the nanoindentation results by the Oliver and Pharr method [23].

3 Results and discussion

3.1 Crystal structure analysis

X-ray diffraction pattern of an as-deposited stainless steel thin film is shown in Fig. 1a. The strong intensity observed for the XRD pattern indicates a high crystallinity of the nanocrystalline thin films. The formation of nanocrystal can be assigned to the fast cooling of the hot atomic vapour when deposited on a cooled substrate [16]. This process can be compared to the formation of nanoclusters by inert gas condensation, where cooling of the hot atoms was achieved by cooled inert gas [24, 25]. Table 3 shows a comparison between the diffraction peaks in the figure and the reported values using JCPDS card number 6–696. Those results demonstrate that the as-prepared stainless steel thin films are primarily composed of ferrite with α-phase of BCC. In addition, the experimental values of the position of the diffraction peaks in Table 3 reveal a shift towards higher 2θ angles ($\delta\theta = 0.034$) compared to the pure ferrite. This indicates that the ferrite network is distorted, most probably because the ferrite is allied with other elements (nickel, manganese, and chrome). It should be noted here that the XRD results of the as-prepared stainless steel thin films are reproducible regardless of the substrate type; thus, the thin films are well crystallized.

A careful observation at the bottom of the broadening of the (110) peak clearly shows a left asymmetry, indicating the presence of another peak with low intensity that can be attributed to the presence of a secondary phase. A deconvolution of the (110) peak was performed using the Diffract-Plus software with "pseudo-Voigt" function, and it reveals the presence of additional peak (111) that belongs to the γ-phase of FCC structure, as shown in Fig. 1b. This indicates that the as-prepared stainless steel thin films have

Table 2 Values of ψ angle used to determine the residual stress

N°	1	2	2	4	5	6	7	8	9
ψ (°)	−39.2	−33.2	−26.2	−18.4	0	+18.4	+26.2	33.2+	+39.2

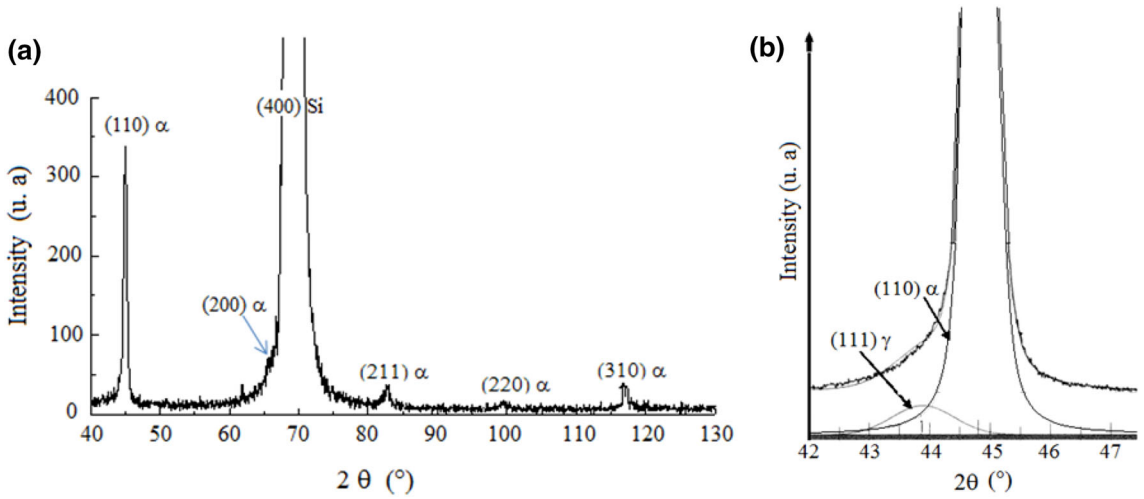

Fig. 1 **a** XRD pattern of stainless steel nanocrystalline thin film. **b** Separation of the two peaks: (110) α-phase and γ-phase as obtained by deconvolution using a Diffract-plus software

Table 3 Indexing the α-phase using X-ray diffraction peaks for stainless steel film using a standard card (JCPDS number 6-696)

Diffraction peaks		1	2	3	4	5
Experimental XRD pattern	2θ (°)	44.80	65.60	82.59	99.26	117.51
Reference: JCPDS number 6-696 α-phase BCC	2θ (°)	44.674	65.023	82.335	98.948	116.390
	(hkl)	(110)	(200)	(211)	(220)	(310)

Table 4 Indexing the X-ray diagram peaks for α and γ phases for the stainless steel film

Diffraction peaks	2θ (°)	FWHM (°)	I (au)	Reference
(110) α-phase	44.8037	0.5506	510.14	JCPDS N° 6-696, phase: α-BCC
(111) γ-phase	43.8545	1.2052	21.14	JCPDS N°33-397, phase: γ-FCC

a crystalline structure with two phases: α-phase which is the dominant phase and thus it represents the matrix, and γ-phase with low concentration. The parameters of both diffraction peaks (110) α-phase and (111) γ-phase are presented in Table 4. Quantitative phase analysis can be performed using the intensity ratio ($\frac{I\gamma}{I\alpha}$) which is proportional to the volume fraction ratio of the corresponding phase ($\frac{C\gamma}{C\alpha}$) and the ratio of the characteristic coefficients of the considered phases ($\frac{R\gamma}{R\alpha}$), using Eq. (1) [26]:

$$\frac{I\gamma}{I\alpha} = \frac{R\gamma C\gamma}{R\alpha C\alpha} \tag{1}$$

The intensity of each phase in Table 4 is given in arbitrary units (au). The quantitative microstructural analysis of the stainless steel thin films reveals that ∼94 % of the thin films are of α-phase and ∼6 % are of γ-phase, as shown in Table 5. Moreover, the crystal size can be estimated using Scherrer's relation applied for the (110) α-peak [10]:

$$D = \frac{K\lambda}{\beta \cos\theta} \tag{2}$$

where D is the average diameter of a crystal, β is full width at half maximum of the diffracted line (FWHM), θ is Bragg angle, λ is the incidental wavelength of Cu anode, and K is a constant that depends on the crystal shape. In the present study, $K = 1$ is used since the thin films contain dual crystal structures. The calculated values for the crystal size are given in Table 6. The obtained values of nanocrystal diameter ($D_\alpha = 17$ nm and $D_\gamma = 8$ nm) confirm that the as-prepared stainless steel thin films produced by thermal evaporation consist of nanometre-sized crystals.

Table 5 Quantification of the α and γ phases using Eq. (1)

Intensities ratio (Iγ/Iα)	Coefficients ratio (Rγ/Rα)	Quantity of each phase	
		Cγ	Cα
∼0.042	∼0.693	∼6 %	∼94 %

Table 6 Crystallite size values α and γ phases present in the stainless steel nanocrystalline thin film calculated using the X-ray diffraction pattern

Phases	(hkl)	2θ (°)	B (rd)	D (nm)
Ferrite (α)	(110) BCC	44.8	0.0096	17
Austenite (γ)	(111) FCC	43.85	0.0209	8

3.2 Surface analysis

The surface morphology of the stainless steel nanocrystal thin films is investigated by SEM and optical metallographic microscope (using a CCD camera coupled to a computer equipped with "Visilog" software for image processing). Figure 2 presents the surface morphology of a nanocrystal thin film. The images show that the films are free of apparent defects or microscopic cracks. The optical micrograph in Fig. 2a shows a smooth and uniform surface, with a homogeneous and regular texture. The SEM micrograph in Fig. 2b shows a fine granular-shaped film with the presence of small grown islands.

3.3 Chemical composition

The results of elemental chemical analysis carried out by EDX are presented in Table 1. The table shows that the chemical composition of the nanocrystal thin films is close to that of the initial bulk material. The observed increase in the concentration of Mn for thin films is due to its high evaporation rate generated by the low vapour pressure of this element and its low evaporation temperature (800 °C) compared to that of the remaining metals under high vacuum (for Fe ∼1000 °C, Cr ∼1300 °C, and Ni ∼1100 °C) [27]. However, concentrations of Cr and Ni in the stainless steel thin films are almost identical to that of the bulk. Herein, the high vacuum in the deposition chamber (10^{-6} mbar) interrupts the oxidation reaction of iron (FeO + C = CO + Fe) [28]; thereby, a decarburization without oxidation of chromium occurs within the nanocrystal stainless steel thin films [29]. Accordingly, Cr and Ni concentrations are conserved in the thin films, while carbon concentration is reduced [30]. It should be noted here that the concentrations of Si and C in thin films could not be quantified as their concentrations are below the resolution of the EDX.

3.4 TEM analysis

The TEM observations of the stainless steel nanocrystal thin films that include the micrographic structure and diffraction patterns are shown in Figs. 3 and 4. Figure 3a shows a TEM image in the bright field mode that reveals a polycrystalline structure with nanocrystals of sizes (25–28 nm) and random orientation. The nanocrystal sizes have a normal distribution, and they are of the same order of magnitude of the sizes obtained by the XRD analysis. Nevertheless, size calculation by XRD analysis produces a rough and qualitative estimation of nanocrystal size, while TEM images produce accurate size within the accuracy of the microscope.

The examination of the TEM electron diffraction patterns (Figs. 3b, c, 4a, b) reveals the phases present in the stainless steel thin films (by indexing the diffraction rings and relating them to the phases, which allows determination of crystal parameters of the considered phase). Herein, TEM was used in the dark field mode where only crystal diffraction patterns appear in the figure. The diffraction rings in Fig. 3b confirm all crystal planes associated with stainless steel of α-phase, in agreement with Table 3. The excessive width of the central ring diffraction diagrams in

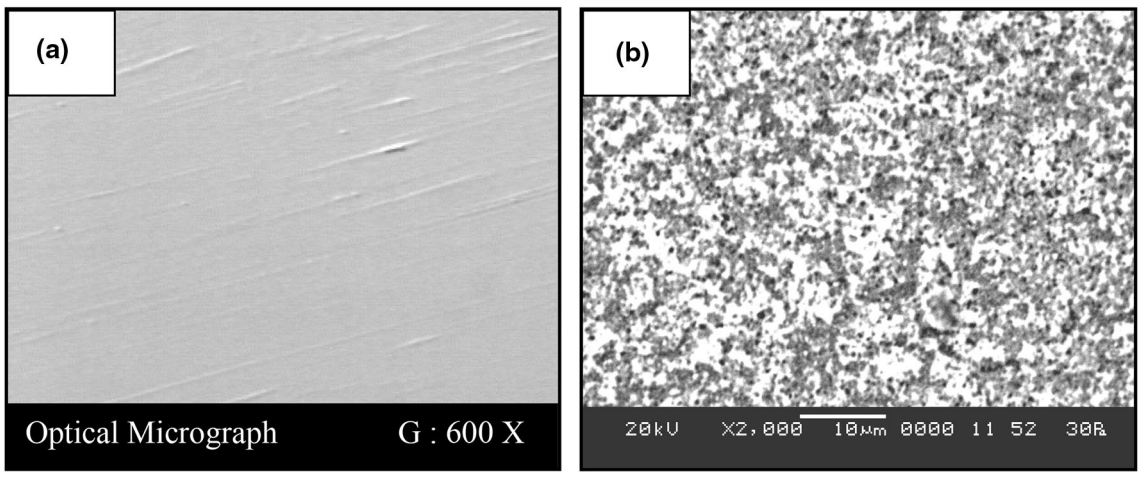

Fig. 2 Representative surface aspects of stainless steel nanocrystalline thin films. **a** Optical micrograph; **b** SEM micrograph

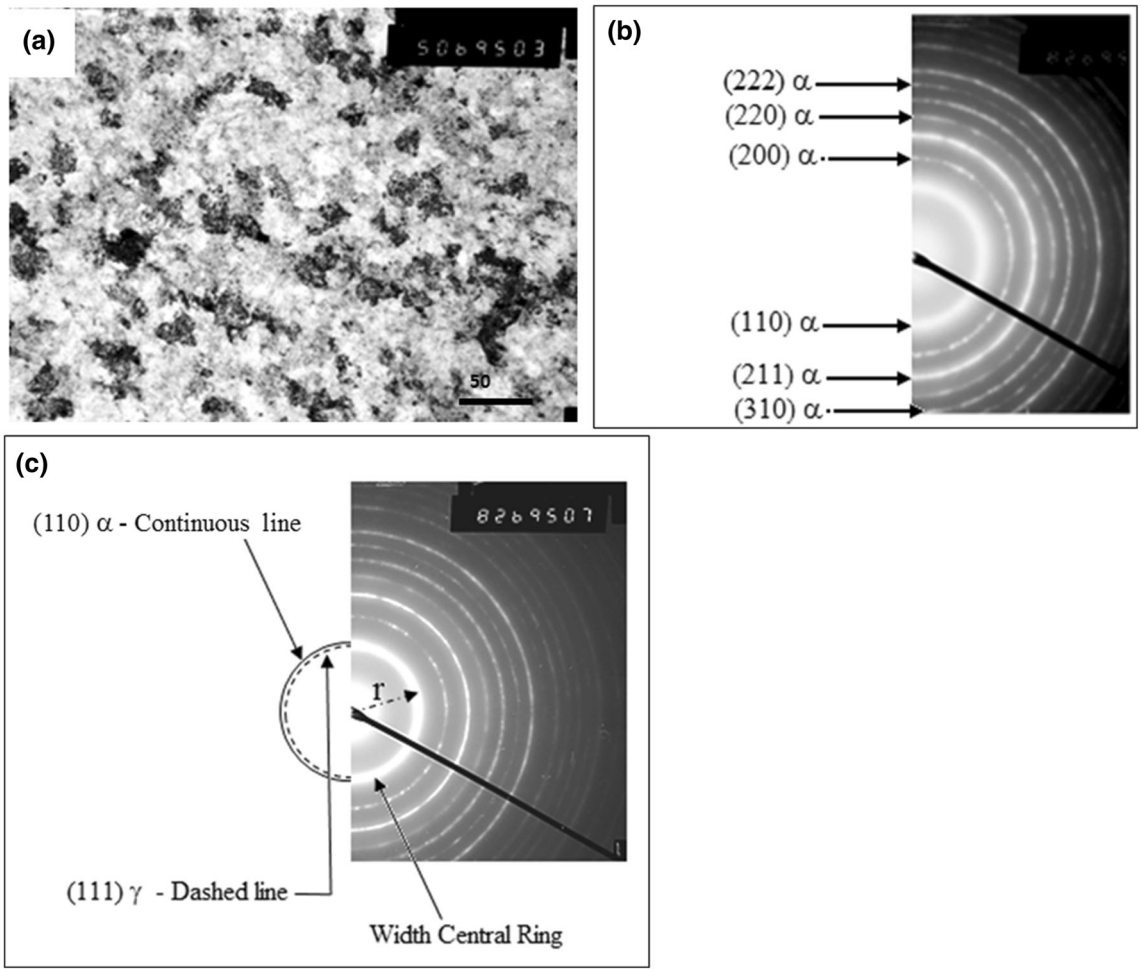

Fig. 3 **a** TEM image of a stainless steel thin film. **b** A diffraction pattern that reveals all atomic planes of α-phase. **c** A diffraction pattern that reveals the existence of both phases: α and γ. *Right* experimental rings. *Left* theoretical rings

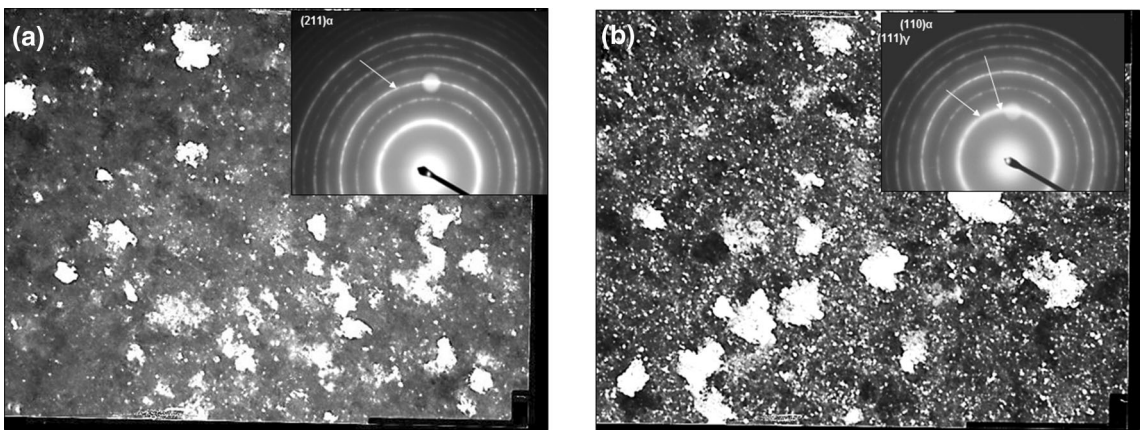

Fig. 4 Micrographs in dark field of the stainless steel thin film structure revealing the (211) of α-phase (**a**), as well as (110) of α-phase and (111) of γ-phase (**b**).

Figs. 3 and 4 reveals the presence of juxtaposition of rings corresponding to (111) of γ-phase and (110) of α-phase (along with the other rings of α-phase). The dark field image of Fig. 4a shows bright crystals that correspond to the diffraction ring of α-phase for (211) electronic diffraction pattern. In addition, the dark field image of

Table 7 Experimental and theoretical parameters of (d_{hkl})

Parameters d_{hkl} (Å)				
Width of the central ring for electron diffraction pattern	Rings of reference JCPDS files		Experimental results from XRD	
	6–696	33–397		
2.046	2.027 (110) α	2.075 (111) γ	2.0205 (110) α	2.0619 (111) γ

Fig. 4b shows more bright crystals that correspond to both diffraction rings of γ-phase and α-phase for (111) and (110) electronic diffraction patterns, respectively. The crystal parameter values are presented in Table 7, which confirm the presence of the two phases: α and γ. These results are consistent with the results obtained by XRD and CEMS (as below) methods.

3.5 CEMS analysis

CEMS spectrum of a stainless steel nanocrystal thin film deposited on a Si substrate (166 nm thick) is presented in Fig. 5. The figure reveals a ferromagnetic sextuplet composed of six wide lines and a paramagnetic singlet in the centre with variable intensities. The ferromagnetic and paramagnetic components confirm the presence of α (ferromagnetic) and γ (paramagnetic) phases. The values of isomeric displacements (IS) of the ferromagnetic and paramagnetic parts of the spectrum are 0.034 and −0.14 mm/s, respectively. It should be noted here that the IS values of the stainless steel film films are larger than that of standard bulk iron due to the higher Ni concentration in the BCC α-phase. Also, the IS values of the stainless steel films are less than that of bulk 304 stainless steel due to the higher Cr concentration in the FCC γ-phase. The above CEMS spectrum supports that stainless films obtained by thermal evaporation process an unstable polycrystalline structure that consists of FCC γ-phase that is formed in small quantity (about 10 % of iron atoms), and the majority is BCC α-phase. Also, after deconvolution of the CEMS spectrum, two local environment (ferromagnetic iron) sites in the BCC α-phase ferromagnetic were revealed in Fig. 5: (i) s1 that represents the spectrum that corresponds to local environment site which is strongly ferromagnetic and rich in Cr; and (ii) s2 that represents the spectrum corresponds to local environment site that is weakly ferromagnetic and rich in Ni and Mn.

3.6 Magnetism

The temperature dependence of the magnetization for the fabricated stainless steel thin films measured at 50 Oe is shown in Fig. 6. The figure reveals a direct increase in the

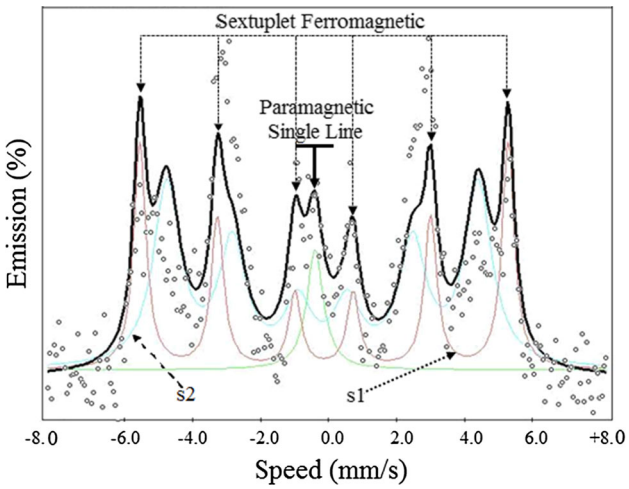

Fig. 5 CEMS spectra at ambient temperature for various nanocrystalline stainless steel thin films. The spectrum corresponding to first environment site (s1) that is strongly ferromagnetic in BCC α-phase. The s1 site is rich in Cr. The spectrum corresponding to second environment site (s2) that is weakly ferromagnetic in BCC α-phase. The s2 site is rich in Ni

magnetization with temperature. The increase in magnetization with temperature is assigned to the majority of the ferrite phase within the thin films as illustrated above. In contrary, for different systems with major concentration of austenite, the magnetization was reported to either decrease [31] or increase and then decrease [32]. The magnetization curves at 5 and 300 K are shown in Fig. 7. The hysteresis reveals strong magnetic properties which are consistent with the domination of the ferrite phase with the thin films [31]. As the temperature increases from 5 to 300 K, the coercivity increases from about 50–90 Oe, and the saturation remanence increases from 0.00085 to 0.00095 emu/cm^3. Those figures are consistent with the structural and compositional results discussed above.

3.7 Residual stress

The residual stress was evaluated by the analysis of a single Debye ring via the conventional $\sin^2 \psi$ method. The $\sin^2 \psi$ method was applied to the (211) diffraction line of the ferrite (α-phase) stainless steel thin film, which corresponds to the angle $2\theta = 82.696°$. The peak position is largely influenced by the value and direction of the residual stress developed in these thin films. The results of the residual stress analyses are represented in Fig. 8. The figure shows the development of two groups of straight line fitting for $\ln(1/\sin \theta)$ as a function of ($\sin^2 \psi$). Only slight difference between the slopes of the two groups can be observed. Both fittings define the intensity and the direction of residual stresses developed in these stainless steel thin films which proves that the residual stresses are biaxial

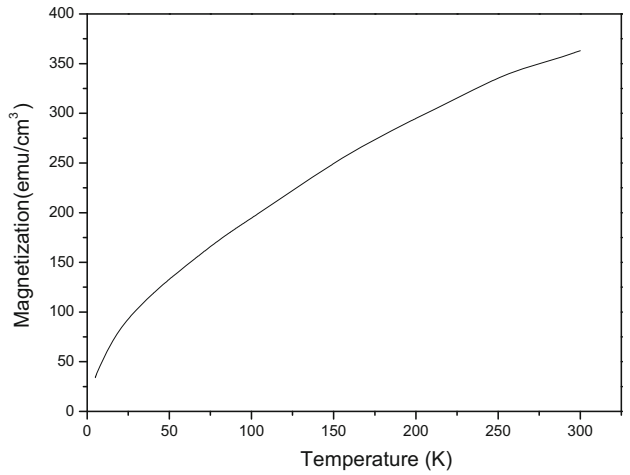

Fig. 6 Magnetization as a function of temperature for a stainless steel thin film

with out-of-plane normal stress; i.e. $\sigma_3 = 0$ (σ_3 is the following constraint to the vertical z-axis on the surface). Accordingly, no stress gradient is applied for the studied thin films because of the minimal difference between the two orientation branches ($-\psi$ and $+\psi$). The slope (m) of the linear fit of $\ln(1/\sin\theta)$ versus ($\sin^2\psi$) is $m = \frac{1}{2} S_2 \sigma\varphi$. Here, $\frac{1}{2} S_2 = 5.71 \times 10^{-3}$ (1/GPa), and $m = 0.0103$. This permits the evaluation of the residual stress value, and it is equal to $\sigma\varphi = +1.7$ GPa. The residual stress calculated here is of tension with low intensities.

3.8 Hardness and elastic modulus

Hardness and elastic modulus were determined by the nanoindentation test. These mechanical properties at nanometres scale can influence the behaviour and durability of stainless steel thin films in the environmental industries. The test results are presented by the curves tracing the relation between the force applied (F) and the penetration depth (h) of the nanoindenter. This test reveals the evolution of the penetration depth of indenter under the effect of the increasing force applied, and it permits to determine the hardness (H) and elastic modulus (E) of the stainless steel thin films. The results of the nanoindentation test are shown in Fig. 9. The figure shows clearly that the stainless steel thin films have approximately a hardness value of 7.5 MPa and an elastic modulus value of 104 GPa. Evidently, the stainless steel nanocrystal thin films prepared by the thermal evaporation technique exhibit hardness and elastic modulus rather low relative to that of the bulk 304 stainless steel ($E = 200$ MPa). Herein, the weak impact energy of evaporated atoms introduces some faults between nanocrystals, and it develops tensile stress in the nanocrystal thin films; thus, it generates a low elastic modulus and a low hardness and alters all the mechanical properties. This phenomenon can be explained by the atomic peening model, where surface modification is assigned to the collision of many small solid objects with the surface [33].

4 Conclusion

In this work, we optimized the fabrication conditions of stainless steel thin films formed by thermal evaporation; therefore, the crystal structure and chemical composition were reproducible. The thin films exhibit good surface aspect and dual crystal structure: BCC (α-phase) that is ferromagnetic and FCC (γ-phase) that is paramagnetic. The γ-phase was detected by conversion electron Mössbauer spectroscopy (CEMS) and X-ray diffraction (XRD), and its abundance was estimated to be 10 % using CEMS and 6 % using XRD. The thin films exhibit nanocrystal structure with crystal sizes of 17 nm for the α-phase, and 8 nm for the γ-phase. In addition, the thin films obtained by thermal evaporation are not textured because they exhibit rather a

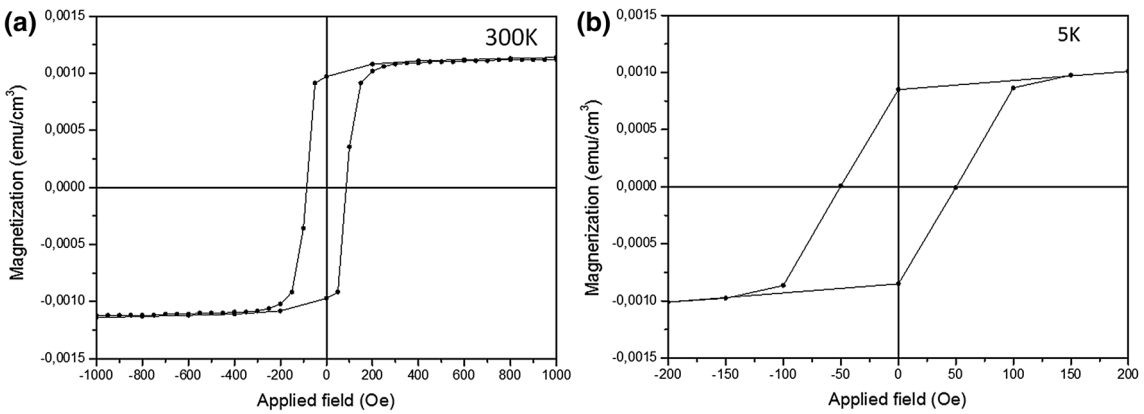

Fig. 7 Magnetization measurements as a function of applied magnetic field performed at (**a**) $T = 300$ K and (**b**) $T = 5$ K

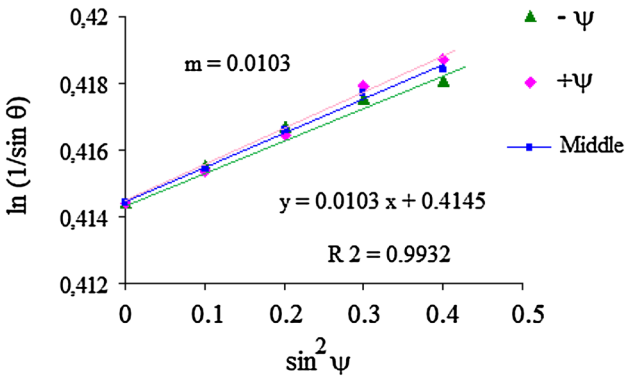

Fig. 8 Dependence of [ln (1/sin θ)] on ($\sin^2 \psi$) applied to the (211) line diffracted of the ferrite (α-phase) thin film. The *straight lines* are linear fits

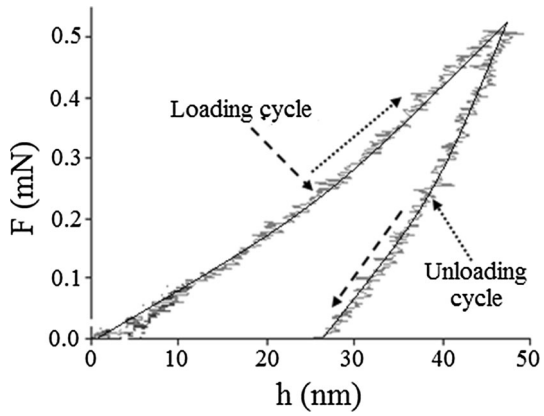

Fig. 9 Nanoindentation test applied on for stainless steel thin films deposited on silicon substrate: evolution of the force applied to penetrate the nanoindenter point versus the penetration depth

small disorientation as revealed by XRD. These stainless steel thin films exhibit residual stress constraints of an average value of 1.7 GPa, hardness of 7.5 MPa, and elastic modulus of 104 GPa. Therefore, the prepared thin films can be utilized for practical industrial applications such as protective coating layers.

References

1. R.M. Fernández-Domene, E. Blasco-Tamarit, D.M. García-García, J. García-Antón, Effect of alloying elements on the electronic properties of thin passive films formed on carbon steel, ferritic and austenitic stainless steels in a highly concentrated LiBr solution. Thin Solid Films **558**, 252–258 (2014)
2. T. Li, L. Liu, B. Zhang, Y. Li, X. Wang, F. Wang, Direct observation of thin membrane passive film over the growing pit on sputtered nanocrystalline austenitic stainless steel film. Electrochem. Commun. **52**, 80–84 (2015)
3. S. Cao, B. Liu, L. Fan, Z. Yue, B. Liu, B. Cao, Highly antibacterial activity of N-doped TiO2 thin films coated on stainless steel brackets under visible light irradiation. Appl. Surf. Sci. **309**, 119–127 (2014)
4. T.C.K. Yang, Y.-L. Yang, R.-C. Juang, T.-W. Chiu, C.-C. Chen. The novel preparation method of high-performance thermochromic vanadium dioxide thin films by thermal oxidation of vanadium-stainless steel co-sputtered films, Vacuum
5. K. Nomura, T. Okubo, M. Nakazawa, Surface analysis of thin stainless steel films and thick-coated steel by simultaneous application of conversion electron and X-ray Mössbauer spectroscopy. Spectrochim. Acta B **59**, 1259–1264 (2004)
6. G. Fu, N.H. Loh, S.B. Tor, B.Y. Tay, Y. Murakoshi, R. Maeda, Injection molding, debinding and sintering of 316L stainless steel microstructures. Appl Phys. A-Mater Sci Proces **81**, 495–500 (2005)
7. L.Q. Guo, M.C. Lin, L.J. Qiao, A.A. Volinsky, Ferrite and austenite phase identification in duplex stainless steel using SPM techniques. Appl. Surf. Sci. **287**, 499–501 (2013)
8. P. Bruesch, K. Muller, A. Atrens, H. Neff, Corrosion of stainless-steels in chloride solution—an XPS investigation of passive films. Appl. Phys. A Mater. Sci. Proces. **38**, 1–18 (1985)
9. K.H. Lo, J.K.L. Lai, J. Magn. Magn. Mater. **322**, 2335–2339 (2010)
10. F. Paraguay, D.W. Estrada, L.D.R. Acosta, N.E. Andrade, M. Miki-Yoshida, Growth, structure and optical characterization of high quality ZnO thin films obtained by spray pyrolysis. Thin Solid Films **350**, 192–202 (1999)
11. T. Li, L. Liu, B. Zhang, Y. Li, X. Wang, F. Wang, Electrochem. Commun. **52**, 80–84 (2015)
12. S. Jin, A. Atrens, Passive films on stainless-steels in aqueous-media. Appl Phys A Mater Sci Proces **50**, 287–300 (1990)
13. K. Oh, S. Ahn, K. Eom, K. Jung, H. Kwon, Corros. Sci. **79**, 34 (2014)
14. M. Kumagai, S.-T. Myung, H. Yashiro, Y. Katada, J. Power Sources **210**, 92 (2012)
15. P. Lacombe, B. Baroux, G. Beranger. Les aciers inoxydables, Les éditions de physique, Les Ulis, France (1990)
16. S.D. Dahlgren, Metall. Trans. **1**, 3095 (1970)
17. J. Childress, S.H. Liu, C.L. Chien, J. Appl. Phys. **64**, 6059 (1988)
18. F.S. Li, J.J. Sun, C.L. Chien, J. Phys.: Condens. Matter **7**, 1921 (1995)
19. J.P. Eymery, G. Laplanche, M. Cahoreau, M.F. Denanot, Thin Solid Films **217**, 1 (1992)
20. J.P. Eymery, N. Merakeb, P. Goudeau, A. Fnidiki, B. Bouzabata, J. Magn. Magn. Mater. **256**, 227 (2003)
21. N. Merakeb, J.-P. Eymeryb, A. Fnidikic, P. Goudeaub, B. Bouzabata, Mater. Lett. **58**, 711–715 (2004)
22. D. Bodin, J.P. Eymery, Nucl. Instrum. Methods B **16**, 424 (1986)
23. W.C. Olivier, G.M. Pharr, J. Mater. Res. **7**, 1564 (1992)
24. A.I. Ayesh, S. Thaker, N. Qamhieh, H. Ghamlouche, Size-controlled Pd nanocluster grown by plasma gas-condensation method. J. Nanopart. Res. **13**, 1125 (2011)
25. A.I. Ayesh, N. Qamhieh, H. Ghamlouche, A.M.E.-S.S. Thaker, Fabrication of size-selected Pd nanoclusters using a magnetron plasma sputtering source. J. Appl. Phys. **107**, 034317 (2010)
26. F.S. Khokhar. Quantitative analysis of multi-phase systems—steels with mixture of ferrite and austenite. Linköping University (2005)
27. S. Dushman, *Scientific Foundations of Vacuum Techniques*, 1st edn. (Wiley, New York, 1949)
28. D.C. Hilty, R.H. Taylor, R.H. Gillespie, Predicting minimum materials cost for stainless steel. J Metals **11**, 458 (1959)
29. H. Mass, F.J. Hahn, H. Hyssen, A.G. Hatigenn, *Tendance actuelle* (Colloque européen de métallurgie sous vide, Villeneuve, 1979)
30. H. Mass, F.J. Hahn, H. Hyssen, A.G. Hatigenn. Purification of BOF steel and electric arc steel by RH vacuum treatment.

Colloque Européen de Métallurgie sous vide: "Tendance Actuelle". Villeneuve, 1979. p.61–73
31. T. Garcin, S. Rivoirard, C. Elgoyhen, E. Beaugnon, Experimental evidence and thermodynamics analysis of high magnetic field effects on the austenite to ferrite transformation temperature in Fe–C–Mn alloys. Acta Mater. **58**, 2026–2032 (2010)
32. S.K. Putatunda, S. Unni, G. Lawes, Mechanical and magnetic properties of a new austenitic structural steel. Mater. Sci. Eng., A **406**, 254–260 (2005)
33. H. Windischmann, Crit. Rev. Solid State Mater. Sci. **17**, 547 (1992)